

Cooperative deformation mechanisms in a fatigued CoCrNi multi-principal element alloy: A case of low stacking fault energy

Kaiju Lu^{a,*}, Ankur Chauhan^b, Dimitri Litvinov^a, Mike Schneider^c,
Guillaume Laplanche^d, Jarir Aktaa^a

^a Institute for Applied Materials, Karlsruhe Institute of Technology (KIT), Hermann-von-Helmholtz-Platz 1, 76344 Eggenstein-Leopoldshafen, Germany

^b Department of Materials Engineering, Indian Institute of Science, Bengaluru, 560012 Karnataka, India

^c Chimie ParisTech, CNRS, Institut de Recherche de Chimie Paris, PSL University, 75005 Paris, France

^d Institut für Werkstoffe, Ruhr-Universität Bochum, D-44801 Bochum, Germany

A B S T R A C T

Keywords:

Multi-principal element alloys
Fatigue
Deformation mechanisms
Dislocation
Transmission electron microscopy (TEM)

Multi-principal element alloys (MPEAs) of low stacking fault energies (SFEs) often exhibit outstanding damage tolerance. In contrast to the well-understood monotonic deformation behaviors, fatigue deformation mechanisms of the low-SFE MPEAs remain fundamental questions. Using TEM, this work demonstrated two main dislocation configurations cooperating in an exemplary low-SFE CoCrNi MPEA, namely slip bands and veins/walls/cells, which are usually formed in materials with low- and high-SFEs, respectively. Under low strain amplitude of 0.3%, the deformation features are found to include primary and double slip bands (dominating in $\approx 71\%$ and 29% grains, respectively). Upon increasing strain amplitude, apart from the slip bands, dislocation substructures formed (*i.e.*, veins/walls/cells present in $\approx 33\%$ and 60% grains under strain amplitude of 0.5% and 0.7%, respectively) due to cross slip, despite the alloy's low-SFE. Moreover, the slip bands and walls/cells are found to serve more likely as geometrically necessary dislocations and statistically stored dislocations, respectively. Besides, the constraints from neighboring grains and Copley-Kear effect (rather than grain orientation) were suggested to play more important role in determining these dislocation patterns formation. Lastly, this work evidenced unexpected partial dislocations and stacking faults (in addition to usually observed screw dislocations) shuttling between the walls/cells by planar slip. This predominant planar slip behavior explains well the exceptional damage tolerance of low-SFE MPEAs. These insights can also advance the understanding of fatigue deformation of conventional alloys with low-SFEs.

1. Introduction

Multi-principal element alloys (MPEAs) have attracted tremendous attention due to their unique atomic structures and promising mechanical properties (Cantor et al., 2004; Cao, 2022; Gludovatz et al., 2014, 2016; Hua et al., 2021; Laplanche et al., 2017; Liu et al., 2022; Ming et al., 2019; Pan et al., 2021). Within the numerous MPEA systems, CoCrNi-based face-centered cubic (FCC) MPEAs have been extensively investigated, owing to their excellent strength, ductility, and fracture resistance (Gludovatz et al., 2014, 2016;

* Corresponding author.

E-mail addresses: kaiju.lu@hotmail.com, kaiju.lu@kit.edu (K. Lu).

Laplanche et al., 2016, 2017; Wagner and Laplanche, 2023b). Among them, CoCrNi exhibits the best mechanical properties, which are primarily rooted in its low stacking fault energy (SFE) and exceptional strain hardening, e.g., as compared to CoCrFeMnNi alloy (Gludovatz et al., 2016; Laplanche et al., 2017; Wagner and Laplanche, 2023a). Despite the well-understood strength-ductility properties of CoCrNi-based MPEAs (Gludovatz and Ritchie, 2022), intriguing questions remain as to how they perform under cyclic loading and what are their fundamental fatigue deformation mechanisms. These questions are critical for their potential engineering applications (Lavenstein et al., 2020; Stinville et al., 2022), as 80% of all engineering alloy failures are estimated to arise from fatigue (Suresh, 1998).

For conventional FCC materials, the plastic deformation during the early stages of fatigue is usually accommodated by dislocation slip (Mughrabi, 1983; Sangid, 2013). Upon further cycling, dislocations rearrange into low-energy patterns, which are often responsible for the fatigue crack initiation stage (Sangid, 2013) and consume most of the fatigue lifetime (e.g., 78%–85% of the lifetime in a widely used 316 L steel (Oliveira et al., 2022)). The low-energy dislocation patterns generally can be divided into two groups of dislocation substructures. One group is so-called planar slip bands, also called persistent Lüder bands (PLBs), high-density dislocation walls (HDDWs), see Fig. S1A. These slip bands are believed to originate from dislocation planar slip and usually observed in materials with low SFEs (Heczko et al., 2017; Li et al., 2019; Lu et al., 2021b; Shao et al., 2017; Yan et al., 1986). The other group of low-energy dislocation substructures includes the well-known dislocation veins, walls (also called persistent slip bands) and cells, which form due to cross slip, accommodate different amounts of plastic strain, and are mainly found in materials with medium-to-high SFEs (Buque, 2001; Lavenstein et al., 2020; Mughrabi, 1983; Pham et al., 2013; Suresh, 1998; Winter et al., 1981). In this context, the CoCrNi and CoCrFeMnNi have been considered model low-SFE and medium-SFE MPEAs, respectively, due to their different SFEs (e.g., $22 \pm 4 \text{ mJ/m}^2$ (Laplanche et al., 2017) for CoCrNi and $30 \pm 5 \text{ mJ/m}^2$ (Okamoto et al., 2016; Wagner et al., 2022) for CoCrFeMnNi).

So far, in contrast to the well-established fatigue deformation mechanisms of the medium-SFE MPEAs, e.g., CoCrFeMnNi (Feng et al., 2021; Lu et al., 2020, 2021a, 2022a; Luo et al., 2022; Picak et al., 2020; Shams et al., 2020), the corresponding knowledge for low-SFE MPEAs has remained a largely unexplored territory (Heczko et al., 2021; Lu et al., 2021b; Sisodia et al., 2023). Our previous fatigue study on the low-SFE CoCrNi (Lu et al., 2021b) revealed its superior resistance compared to CoCrFeMnNi, which was mainly attributed to CoCrNi's relatively uniform deformation (i.e., slip bands under a medium strain amplitude of 0.5%). Later on, the formation of slip bands was associated with fatigue crack initiation in CoCrNi during the initial cycles (Heczko et al., 2021). By further comparing to other MPEAs and common FCC steels with low-SFEs, we found that the CoCrNi maintains exceptional fatigue resistance (Fig. 1A-B).

Apart from the SFE, other parameters (such as the applied strain amplitude, cycle number, and grain orientation) can also affect dislocation pattern formation (Lu et al., 2021a; Nellessen et al., 2015; Vakili et al., 2020). Specifically, grain orientation was reported to govern dislocation pattern formation in FCC single crystals (Li et al., 2011), while its influence in polycrystals is still a matter of debate. For example, a significant effect of grain orientation was reported in several low-SFE alloys (Li et al., 2019; Vakili et al., 2020), but not in CoCrFeMnNi (Lu et al., 2021a). Therefore, it is imperative to investigate the influences of these parameters on the operating deformation mechanisms in low-SFE MPEAs, which are essential for microstructure-based modeling.

Consequently, this work aims to deepen the understanding of the fatigue deformation mechanisms (with emphasis on elementary dislocations involved) of the low-SFE CoCrNi MPEA at room temperature (RT) using transmission electron microscope (TEM). This work will serve as a reference for understanding the fatigue deformation mechanisms of conventional low-SFE alloys in general.

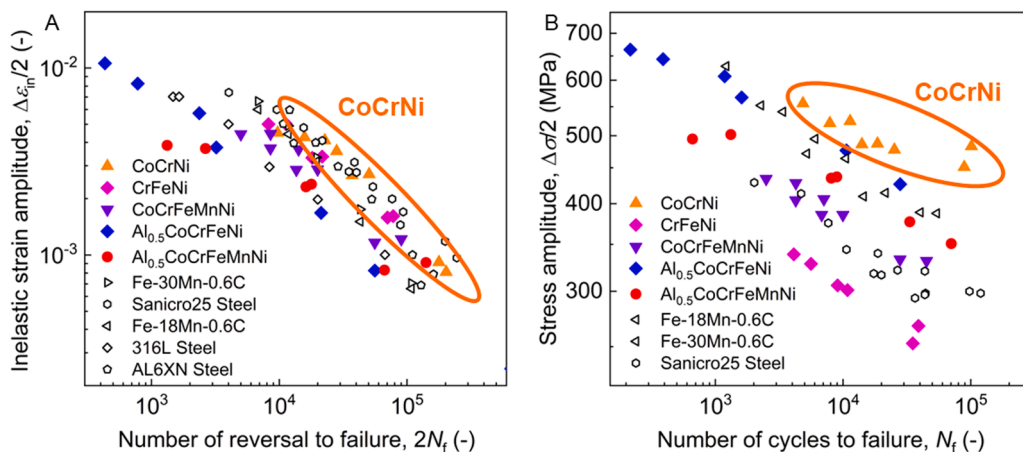


Fig. 1. (A) Manson-Coffin curve and (B) Wohler curve of the CoCrNi alloy and comparisons to other alloys and FCC steels. Compared to several MPEAs and austenitic steels (including CoCrFeMnNi (Lu et al., 2021b), CrFeNi (Sisodia et al., 2023), $\text{Al}_{0.5}\text{CoCrFeMnNi}$ (Lu et al., 2022b), $\text{Al}_{0.5}\text{CoCrFeNi}$ (Feng et al., 2021), high-Mn TWIP steel (Shao et al., 2016), AL6XN steel (Li et al., 2019), Sanicro25 (Polák et al., 2014), and 316 L steel (Oliveira et al., 2022)), CoCrNi (Lu et al., 2021b) exhibits excellent fatigue resistance.

2. Materials and methods

2.1. Material

Starting from pure metals (purity ≥ 99.9 wt.%), an equiatomic CoCrNi alloy was produced by induction melting, casting, homogenization, and rotary swaging. The details can be found in Refs. (Laplanche et al., 2017; Lu et al., 2021b). Fatigue specimens (with gage length and diameter of 7.6 mm and 2 mm, respectively, see Fig. S2) were machined out from the rotary-swaged rods, with their loading axis parallel to the longitudinal direction of the rods. Afterwards, the specimens were axially polished to remove the circumferential tool marks developed during the previous turning step. This polishing step ensures a surface roughness of $\sim 0.26 \pm 0.03$ μm , which is comparable to that of CoCrFeMnNi and $\text{Al}_{0.5}\text{CoCrFeMnNi}$, thus excluding any influence of surface finish on fatigue life comparison in Fig. 1A-B. Finally, the specimens were recrystallized at 1098 K for 1 h after the polishing. As a result, the alloy exhibits a weak $\langle 111 \rangle$ and $\langle 100 \rangle$ texture (along the rod's longitudinal axis), equiaxed grain morphology (with average grain size of ~ 7 μm), a low dislocation density and a relatively high-density of annealing twins, see Fig. S3 (Laplanche et al., 2017; Lu et al., 2021b; M. Schneider et al., 2020). Here, the mean width of the annealing twins is ~ 1.1 μm and, on average, there are ~ 1.3 annealing twin boundary per grain (Schneider et al., 2019, 2020).

2.2. Fatigue testing

Fatigue tests were performed using an MTS 810 servo-hydraulic testing machine equipped with a 7-mm gage length extensometer. The abovementioned fatigue specimens were screwed into two adapters, which were mounted into the grips of the testing machine. A symmetrical triangular waveform ($R = -1$) was employed at a nominal strain rate of $3 \times 10^{-3} \text{ s}^{-1}$. The strain-controlled fatigue tests were conducted in air at RT under different strain amplitudes (0.3%, 0.5%, and 0.7%) until failure. It should be mentioned that the fatigue life and cyclic stress response (*i.e.*, initial cyclic hardening, followed by softening and a near steady state, see Fig. S4) of CoCrNi have been reported in Ref. (Lu et al., 2021b). To further understand the reasons for its cyclic stress response, fatigue tests conducted under 0.5% strain amplitude were interrupted after 20 and 500 cycles to investigate the microstructural evolution.

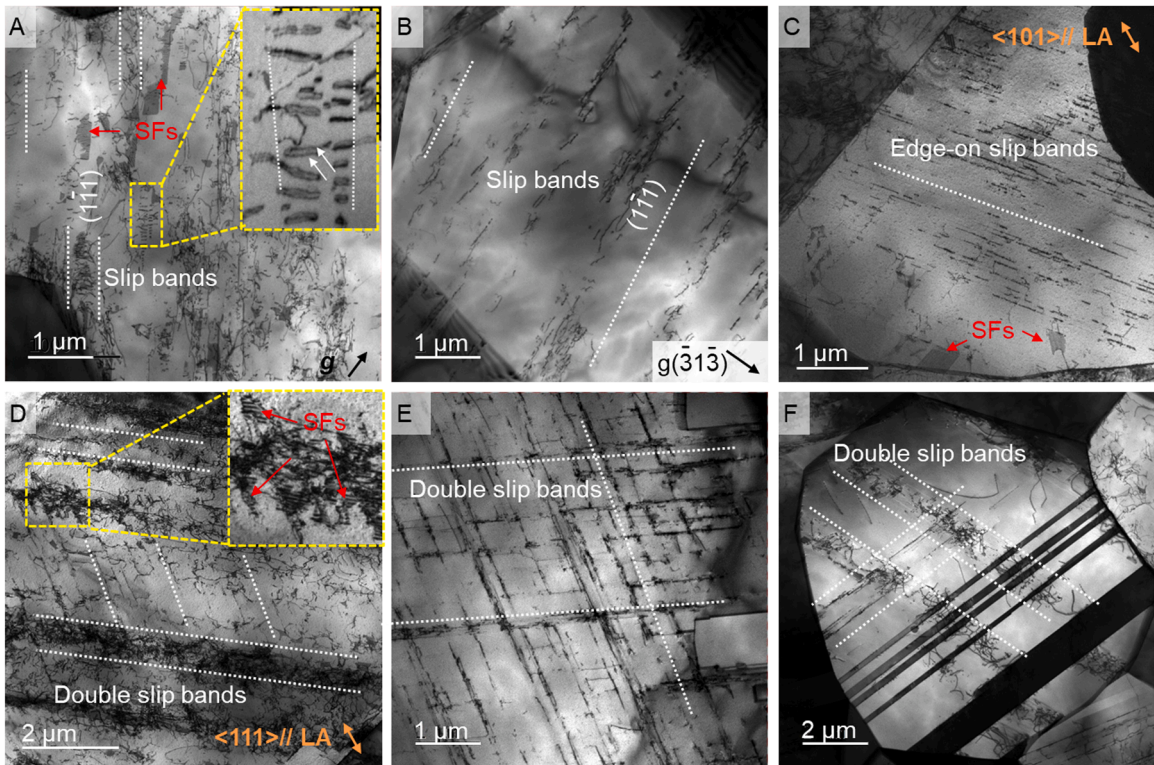


Fig. 2. BF-TEM micrographs of the CoCrNi alloy tested under 0.3% strain amplitude up to fracture. Here, typical dislocation structures are slip bands: (A-C) primary slip bands and (D-F) double slip bands. The straight dotted lines in (A, B, D, F) are parallel to traces of the $\{111\}$ slip plane, which are edge-on in (C, E).

2.3. Microstructural characterization

To obtain post-fatigued microstructures, conventional bright-field (BF) and weak-beam dark-field (WBDF) imaging were employed using an FEI Tecnai F20 TEM microscope operating at 200 kV. TEM samples were prepared by mechanical grinding, polishing, and twin-jet electropolishing (Lu et al., 2021b). During TEM investigations, the dislocation structures were observed using different two-beam diffraction conditions with a standard Gatan double tilt holder. Thereafter, $g\mathbf{b}$ analysis (where \mathbf{g} is the diffraction vector) was employed to determine the Burgers vectors \mathbf{b} of the dislocations (Lu et al., 2021a), see Table S1. Besides, the orientation of the investigated grains was determined by capturing the diffraction pattern (DP), which was then related to the loading axis (LA) of the fatigue specimens.

Furthermore, electron backscattered diffraction (EBSD) investigations were also performed. The details on the EBSD sample preparation and scanning conditions (such as step size of 0.2 μm) can be found in (Lu et al., 2021b). Here, the grain average misorientation (GAM) map was obtained to reflect local misorientations at the grain scale. Specifically, the misorientation between each neighboring pair of points within the grain is calculated. Then the average misorientation value is determined and assigned to each pixel within each grain.

3. Results

3.1. Microstructures after cycling under 0.3% strain amplitude

Fig. 2 provides typical microstructures of the post-fractured CoCrNi tested under 0.3% strain amplitude. The dislocation density strongly increased after cycling compared to the recrystallized state (Fig. S3). The typical deformation-induced microstructure consists of dislocation-rich slip bands (separated by dislocation-free channels) and extended SFs (Fig. 2A-C). Furthermore, these slip bands can be divided into primary slip bands (i.e., oriented on the $\{111\}$ primary slip plane, see Fig. 2A-C) and double slip bands (i.e., oriented on two different $\{111\}$ slip planes, see Fig. 2D-F). Statistically, the primary slip bands are present in $\approx 71\%$ of the investigated grains (i.e., 40 out of 56 grains), with the rest $\approx 29\%$ grains occupied by double slip bands, see Table 1). Besides, both slip bands were found to contain arrays of partial dislocations (bounded by SF ribbons, see inset of Fig. 2A and D).

3.2. Microstructural evolution under 0.5% strain amplitude

Fig. 3 shows representative microstructures of the ruptured CoCrNi alloy that was tested under a strain amplitude of 0.5%. Like that under 0.3% strain amplitude, here, the predominant dislocation structures also include slip bands and extended SFs (Fig. 3A-B). Similarly, $\approx 67\%$ of the investigated grains (54 out of 81 grains, Table 1) exhibit slip bands and SFs. In contrast, with increasing strain amplitude from 0.3% to 0.5%, the dislocation density increases within the slip bands, and the distance between them decreases (e.g., compare Fig. 3A and Fig. 2B-C), both of which originate from higher strain/stress levels. In addition, dislocation veins or irregular walls dominate in the rest of the grains ($\approx 33\%$) under 0.5% strain amplitude (Fig. 3C).

To further reveal the evolution of dislocation structures with cycle number, typical TEM micrographs of CoCrNi alloy tested under 0.5% strain amplitude up to 20 and 500 cycles are shown in Fig. 4A-C and Fig. 4D-F, respectively. The 20 and 500 cycles were chosen as they represent cyclic hardening and softening stages, respectively. After 20 and 500 cycles, the dislocation microstructures consist of slip bands and extended SFs, along with sporadically observed tangles/veins and cross-slip traces (Fig. 4A-E). The yellow arrows in Fig. 4B and D₁ indicate dislocations that cross-slipped from primary slip bands. Furthermore, ill-defined veins or walls started to form after 500 cycles (Fig. 4F), while they were absent after 20 cycles.

3.3. Microstructures after cycling under 0.7% strain amplitude

Fig. 5 displays typical microstructures of post-fractured CoCrNi tested under 0.7% strain amplitude. Here, the main dislocation features include slip bands, extended SFs (Fig. 5A-C), and well-defined wall/cell-like substructures (Fig. 5D-F). Statistically, slip bands and SFs are present in $\approx 40\%$ of the grains (i.e., in 24 out of 59 grains, see Table 1). Here, the character of the SFs (intrinsic vs extrinsic) was determined from a DF micrograph (Fig. 5C) using a procedure developed for FCC materials (Williams and Carter, 1996). When the origin of a \mathbf{g} vector (of type $\langle 111 \rangle$, $\langle 220 \rangle$ or $\langle 400 \rangle$) is placed at the center of the SF in the DF micrograph ($\mathbf{g} = \langle 111 \rangle$ in Fig. 5C), it points away from the bright outer fringe if the fault is intrinsic (or points toward it if extrinsic). If the \mathbf{g} reflection is of $\langle 200 \rangle$, $\langle 222 \rangle$ or $\langle 440 \rangle$, the opposite correlation occurs. As the \mathbf{g} vector ($\langle 111 \rangle$) is pointing away from the bright outer fringe, it is concluded that the SFs in Fig. 5C are intrinsic (rather than extrinsic). This finding is in line with that observed in the monotonically loaded CoCrNi and these

Table 1

Fraction of grains showing distinct dislocation patterns in the CoCrNi alloy: tested under different strain amplitudes (0.3%, 0.5% and 0.7%).

Dislocation patterns	Strain amplitude		
	0.3%	0.5%	0.7%
Primary slip bands and/or stacking faults	$\approx 71\%$	$\approx 67\%$	$\approx 40\%$
Double slip bands	$\approx 29\%$	–	–
Veins, walls or cells	–	$\approx 33\%$	$\approx 60\%$

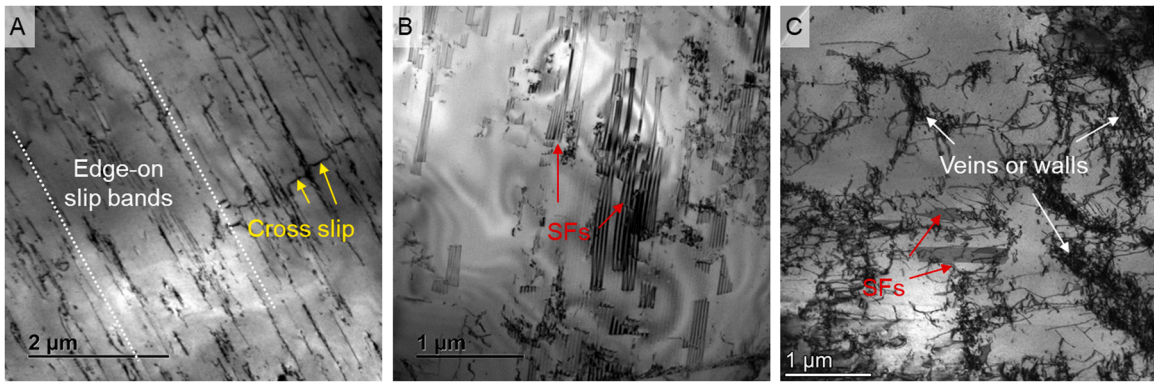


Fig. 3. BF-TEM micrographs of the CoCrNi alloy tested under 0.5% strain amplitude until fracture. Here, typical dislocation features include (A, B) slip bands (SBs) and stacking faults (SFs), (C) and occasionally veins or irregular walls. The straight dotted lines in (A) are parallel to edge-on slip bands.

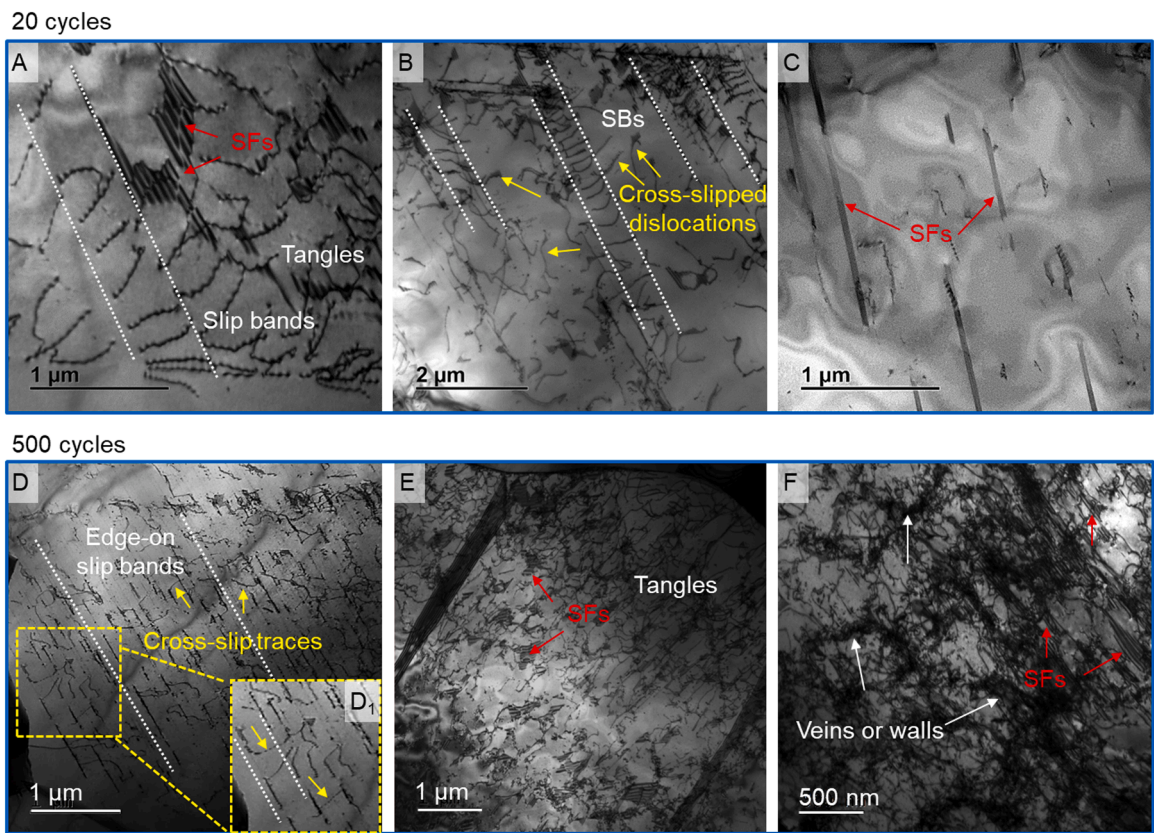
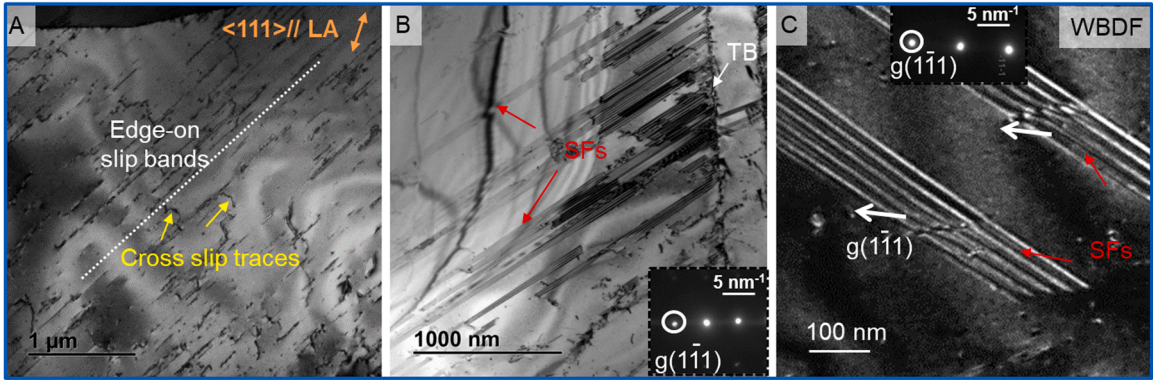


Fig. 4. BF-TEM micrographs of the CoCrNi alloy tested under 0.5% strain amplitude up to (A-C) 20 cycles and (D-F) 500 cycles. After 20 cycles, typical dislocation microstructures consist of (A-C) slip bands (SBs) and stacking faults (SFs), along with occasional tangles and cross-slip traces. After 500 cycles, apart from the above-mentioned features (D-E), ill-defined veins/walls (F) were also observed. The straight dotted lines in D are parallel to the edge-on slip bands.

intrinsic SFs may act as precursor for deformation twinning (DT) (Laplanche et al., 2017). Nevertheless, deformation twins were not observed in the current study, with the reasons discussed in Section 4.1.

Whereas most of the grains are dominated by irregular veins, walls or cells (separated by channels). The corresponding fraction of the grains (60%, under strain amplitude: 0.7%) is significantly higher than that ($\approx 33\%$) observed for a strain amplitude of 0.5%. Interestingly, within the channels (between walls or cells), the following features were identified: (1) extended SFs (see red arrows in Fig. 5E₁), (2) partial dislocations bounded by a narrow SF (see dislocations indicated by red arrows in Fig. S5A₁₋₃), and (3) full

Slip bands or SFs



Cells or walls

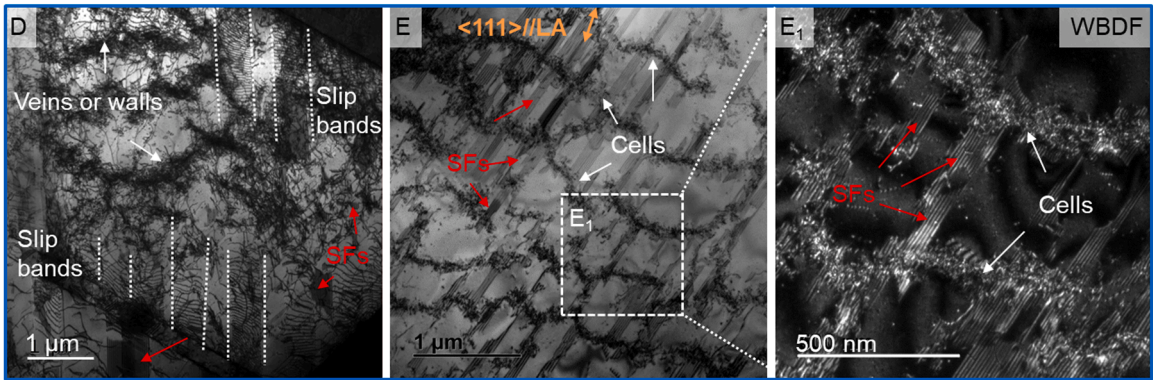


Fig. 5. TEM micrographs of the CoCrNi alloy tested under 0.7% strain amplitude up to fracture. Here, typical dislocation structures include (A-C) slip bands (SBs), stacking faults (SFs), and (D-E) veins, walls or cells. The straight dotted line in (A) is parallel to the edge-on slip band. All micrographs are BF-micrographs, except for (C and E₁), which are WBDF micrographs. The inset in (B-C) are DPs.

dislocations with a screw character (*see* dislocations 1–4 in Fig. S5A₁₋₃, where their screw character is proved by the fact that these dislocations are parallel to $\mathbf{b} = \frac{1}{2} \langle 0\bar{1}1 \rangle$ directions). It should be mentioned that the partials and SFs probably originated from the walls of the cells, and their motion was restricted by the cell size (Fig. 5E₁). More interestingly, only the screw ones (*i.e.*, no SFs and partials) were observed in the channels of CoCrFeMnNi (Lu et al., 2021a) and Copper (Basinski and Basinski, 1992).

In Fig. S5A₁₋₃, $\mathbf{g}\cdot\mathbf{b}$ analyses were performed to identify the Burgers vectors of dislocations in the walls of the cells (in white). However, due to the complexity arising during employing visibility/invisibility criteria on these dislocations, it is challenging to

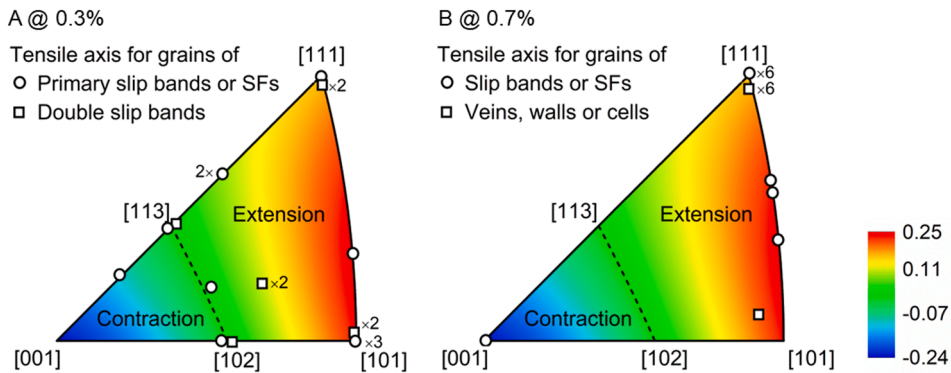


Fig. 6. IPF maps showing orientations (\angle /LA) for grains with distinct dislocation structures in CoCrNi alloy: tested under (A) 0.3% and (B) 0.7% strain amplitudes until fracture. The color bar indicates the difference in Schmid factors on the leading and trailing partials; the line between [102] and [113] separates the regions of extension or constriction of partial dislocations (provided for tension; the opposite trend occurs for compression). The symbol ' × ' next to the square and circle symbols indicates the number of investigated grains showing a specific dislocation structure (*e.g.*, × 2 means that two grains were investigated).

determine the specific Burgers vectors. Nevertheless, as the walls are suggested to develop from dislocation tangles (that could consist of at least two different Burgers vectors), it is reasonable to expect that the walls may also contain dislocations with another Burgers vector. This feature is consistent with the dislocations in walls/cells in CoCrFeMnNi (Lu et al., 2021a).

3.4. Grain orientation effect on dislocation structures

The orientations parallel to the loading axis (LA) of the investigated grains showing either (primary or double) slip bands/SFs or walls/cells for CoCrNi alloy are plotted in the inverse pole figures (IPFs) in Fig. 6. The following distinct observations can be noted. *Firstly*, similar dislocation patterns were formed in grains with different orientations, e.g., slip bands in nearly $\langle 101 \rangle$ and $\langle 111 \rangle$ -oriented grains, also see TEM micrographs in Fig. 2C and Fig. 5A, respectively. *Secondly*, different dislocation patterns were formed in grains with a similar orientation. For instance, individual $\langle 111 \rangle$ -oriented grains exhibited different dislocation microstructures, namely, either primary slip bands/SFs, double slip bands, or walls/cells (also see TEM micrographs in Fig. 5A, Fig. 2D, and Fig. 5E, respectively). In addition, different dislocation patterns (i.e., slip bands/SFs and walls) simultaneously present within the same grains were also observed (Fig. 5D). Therefore, it is concluded that there is a weak correlation between grain orientations and distinct dislocation structures in the polycrystalline CoCrNi alloy. This can be further supported by our EBSD investigations (see Fig. S6 and its caption).

4. Discussion

4.1. Strain-amplitude dependent dislocation structures

This study revealed that the fatigue-induced plastic deformation in the low-SFE CoCrNi is accommodated by slip bands and walls (or cells), which usually compete in different FCC alloys, i.e., the former and latter usually predominate in low and high-SFE alloys, respectively. The observed slip bands, as an indication of planar slip, can be mainly rationalized by the CoCrNi's low-SFE (Lu et al., 2021b). Besides, its high shear modulus of ≈ 90 GPa at RT (Laplanche et al., 2020), stemming from higher atomic bonding, could also promote slip planarity by increasing friction stress and hindering partial dislocations constriction (Hong and Laird, 1990). It is also of interest to note that local chemical short-range ordering, another contributor to dislocation planar slip (Gerold and Karnthaler, 1989), has been considered present in long-term annealed CoCrNi (Zhang et al., 2020) but its role in mechanical properties and SFE was found to be negligible (Li et al., 2022), probably because short-range ordering, if it exists at all, is rapidly destroyed after slip of a few dislocations. Therefore, its role in the current short-term (1 h) annealed CoCrNi is not considered.

It has been reported that slip bands generally involve dislocations from a single (primary) slip system (Li and Laird, 1994) and contain edge dislocations (Inui et al., 1990), see Fig. S1A. In this study, we found evidence of double slip bands (Fig. 2D-F and Fig. 7A) in addition to primary slip bands (Fig. 2A-C). The double slip bands could form the well-known Lomer-Cottrell locks, and hence contribute to the material's hardening. Furthermore, as shown in Fig. 7A, the slip bands were proved to consist of screw dislocations (see cross slip traces in Fig. 4D) as well as dissociated partial dislocations (bounded by SFs, see Fig. 2A and D). Together, this work extends previous understanding of the nature of slip bands in low-SFE alloys after cyclic loading.

It is also noteworthy that, in low-SFE alloys, the frequently observed cross-slip traces (in the channels between slip bands, see Fig. 4D) may contribute to slip band multiplication on parallel slip planes, e.g., by the double cross slip mechanism (Hull and Bacon, 2001). Interestingly, as previously mentioned, cross slip is generally discouraged in low-SFE materials. Nevertheless, it can be enabled in the CoCrNi alloy by high *Escaig* stresses, which may be either induced at stress concentrations (e.g., at the tip of a dislocation pile-up) or by higher applied strain levels during fatigue. Consequently, cross slip is promoted at high strain amplitudes (0.7%), leading to extensive dislocation walls/cells formation. This tendency is akin to medium-to-high-SFE materials (e.g., CoCrFeMnNi) (Lu et al., 2021a; Mayama et al., 2008; Nellessen et al., 2015). However, in contrast to the prevailing cross slip in CoCrFeMnNi (Lu et al., 2021a), cross slip and planar slip coexist in CoCrNi (see Fig. 5D-F).

It should be also mentioned that the alloy's grain size may affect the dislocation structures and hence fatigue properties (Lu et al.,

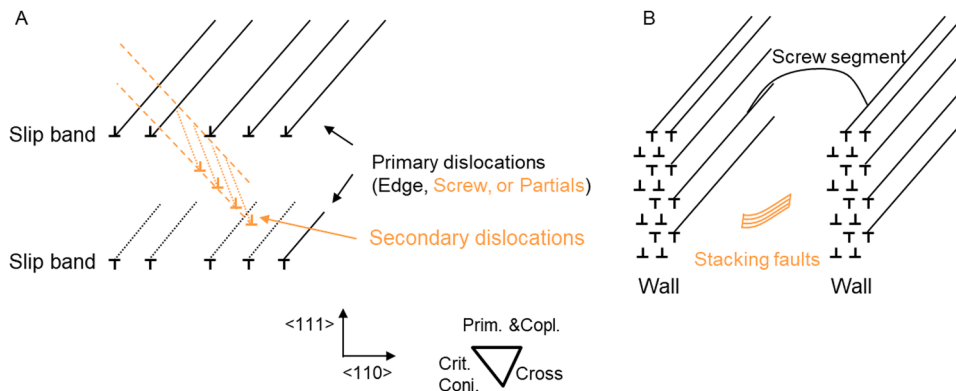


Fig. 7. Schematic illustrations of two typical fatigue-induced dislocation patterns in CoCrNi: (A) slip bands and (B) PSB-walls.

2021a). For instance, it was reported that the dislocation structures become more heterogenous in coarse-grained CoCrFeMnNi (average grain size, $d \approx 60 \mu\text{m}$), *i.e.*, dislocation walls and cells formed more frequently, than in its fine-grained counterpart ($d \approx 6 \mu\text{m}$), which, together with grain boundary strengthening, contribute to the latter's longer lifetime (Lu et al., 2021a). Consequently, it is anticipated that fine-grained CoCrNi exhibit longer lifetime due to grain boundary strengthening and less-heterogenous dislocation structures than its coarse-grained counterpart.

Furthermore, the deformation twinning (DT) was found to occur in the coarse-grained CoCrFeMnNi (but with a limited amount) and not in fine-grained CoCrFeMnNi, which suggests an insignificant role of DT in determining the fatigue properties of CoCrFeMnNi (Lu et al., 2021a). Similarly, no DT was detected by TEM in the fine-grained CoCrNi under the investigated strain amplitudes (from 0.3% to 0.7%). This can be explained by the fact that the critical stress required for the onset of twinning (CTS) has not been reached upon cycling. Specifically, for similar grain-sized CoCrNi, the CTS was reported to be $740 \pm 45 \text{ MPa}$ (Laplanche et al., 2017). Since the maximum peak stress experienced by the present CoCrNi alloy is around $\approx 610 \text{ MPa}$ (under the 0.7% strain amplitude), it is reasonable that no DT was activated herein. Interestingly, another work (Heczko et al., 2021) revealed the DT in the fatigued CoCrNi alloy. This discrepancy may arise from various sources: (1) A larger grain size ($\sim 21 \mu\text{m}$) than in the present work, and (2) a lower SFE ($10 - 20 \text{ mJ/m}^2$ (Shih et al., 2021)), as compared to the present CoCrNi alloy (with grain size of $\approx 7 \mu\text{m}$ and SFE of $22 \pm 4 \text{ mJ/m}^2$ (Laplanche et al., 2017)). It is well-accepted that the CTS decreases with increasing grain size, following a Hall-Petch type relationship (Meyers et al., 2001; Wagner and Laplanche, 2023a); and decreases with decreasing SFE, due to easier separation of full dislocations to partial dislocations. Therefore, these two factors (*i.e.*, larger grain size and lower SFE) contribute to a lower CTS value in the CoCrNi alloy investigated by (Heczko et al., 2021), leading to an easier activation of DT in their material, as compared to the present CoCrNi alloy.

4.2. Estimation of dislocation density and type (GNDs vs SSDs)

Apart from the abovementioned dislocation patterns, it is also of importance to determine the dislocation density of CoCrNi after cyclic loading, which is statistically challenging due to the dense dislocations in the walls and cells as well as the limitation from TEM-based techniques. Here, the total dislocation density was estimated using the Taylor hardening model:

$$\sigma = \sigma_0 + M\alpha Gb\sqrt{\rho} \quad (1)$$

$$\rho = \left(\frac{\sigma - \sigma_0}{M\alpha Gb}\right)^2 \quad (2)$$

where σ is the flow stress, σ_0 is the yield stress ($\sim 411 \text{ MPa}$ for the present CoCrNi, acquired from the stress-strain curve of the first half cycle), M is Taylor factor (3.06), α a geometrical factor (0.125 (Mughrabi, 2016)), G is the shear modulus (90 GPa for CoCrNi (Laplanche et al., 2018)), b the magnitude of the Burgers vector (0.252 nm) and ρ the total dislocation density. It should be additionally pointed out that the geometrical factor α depends on the loading mode, *i.e.*, its value was reported to be $\approx 0.4-0.5$ for monotonic tensile loading (in pure Cu (Mecking and Kocks, 1981) and CoCrFeMnNi (Laplanche et al., 2016) and $\approx 0.1-0.15$ for cyclic loading (Mughrabi, 2016), owing to the different dislocation interactions and resulting dislocation structures.

As the dislocation density remains nearly constant at the near-steady state (Lu et al., 2021a; Luo et al., 2022), its value at the half-life cycle is representative for this stage. By incorporating the applied tensile peak stress σ at the half-life cycle from Fig. S4 in eq. (2), the saturated total dislocation density was estimated (see Fig. 8 and Table S2). It can be seen that the total dislocation density increases significantly with increasing strain amplitude. For instance, with increasing strain amplitude from 0.3% to 0.7%, the dislocation density increases from $\approx 1.20 \times 10^{13} \text{ m}^{-2}$ to $\approx 2.95 \times 10^{14} \text{ m}^{-2}$. Notably, using the Taylor model and the CoCrFeMnNi's data from (Lu et al., 2021a), the estimated dislocation density of CoCrFeMnNi tested under strain amplitude of 0.7% is $\approx 2.60 \times 10^{14} \text{ m}^{-2}$, which is in line with the reported range for CoCrFeMnNi tested under strain amplitude of 1.0% (*i.e.*, $\approx (4 \text{ to } 7) \times 10^{14} \text{ m}^{-2}$,

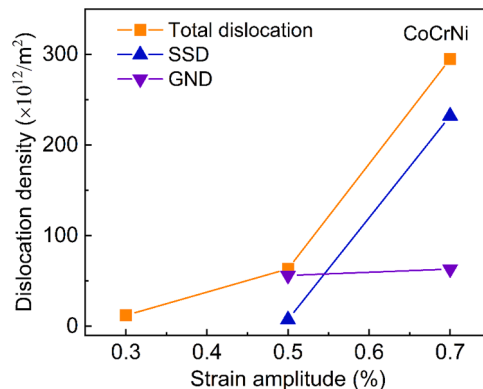


Fig. 8. Estimated total dislocation density, GND-density, and SSD-density of CoCrNi alloy at the steady state tested under different strain amplitudes. The lines are guidelines to the eye only. The GND and SSD densities under strain amplitude of 0.3% were not estimated due to the limited specimens.

obtained by in-situ neutron-diffraction technique (Luo et al., 2022)). Therefore, this consistency verifies the feasibility of the Taylor model to estimate the total dislocation density upon cycling the MPEA.

Furthermore, from the mechanics point of view, it is also important to investigate the contributions of geometrically necessary dislocations (GNDs) and statistically stored dislocations (SSDs) to the total dislocations (Ashby, 1970; Jiang et al., 2013; Zhu et al., 2018). The GNDs density, ρ_{GND} , under strain amplitudes of 0.5% and 0.7% were estimated by EBSD (see Fig. S7) and eq. (2) (Calegnotto et al., 2010) using:

$$\rho_{\text{GND}} = \frac{2\theta}{\mu b} \quad (3)$$

where θ is the kernel average misorientation angle acquired from the EBSD data and μ is the step width (0.2 μm). Notably, the GNDs density noise floor from this method was estimated to be $\approx 5.6 \times 10^{12} \text{ m}^{-2}$ (Jiang et al., 2013).

The SSDs density was obtained by subtracting the GNDs density from the total dislocation density (Zhu et al., 2018).

$$\rho_{\text{SSD}} = \rho - \rho_{\text{GND}} \quad (4)$$

The average densities of GNDs and SSDs are also plotted in Fig. 8 and given in Table S2. Under a strain amplitude of 0.5%, the GNDs take up the majority of total dislocations; while with increasing strain amplitude to 0.7%, the contribution of SSDs far exceeds that of the GNDs (Fig. 8), suggesting rapid non-linear multiplication of SSDs. This indicates that GNDs contribute more to the cyclic strength under low-to-medium strain amplitudes (0.5% and below); while SSDs become more important under higher strain amplitudes (0.7%). This trend agrees well with the finding for monotonically loaded nickel (Zhu et al., 2018) and TWIP steels (Zhi et al., 2020), where the majority of dislocations are GNDs at low initial strains (\approx below 9–14%), while SSDs outnumber GNDs at larger strains due to the rapid non-linear multiplication of SSDs.

4.3. Correlation between dislocation structures and cyclic stress response

The microstructure evolution can be correlated to the previously reported cyclic stress response (*i.e.*, an initial cyclic hardening followed by softening and a near-steady state until failure, see Fig. S4). After 20 cycles, the prevailing slip bands and dislocation tangles (Fig. 4A-C) suggest that the hardening is mainly ascribed to dislocations interaction with grain boundaries (Habiyaremye et al., 2021) and solutes, as well as mutual interactions between dislocations (*i.e.*, forest hardening). Moreover, more frequently observed slip bands (*i.e.*, pile-ups) than tangles (Fig. 4A-C) indicate that dislocation interactions with grain boundaries and solutes outweigh forest hardening at this stage.

After 500 cycles, ill-defined wall substructures (and in-between channels) started to form (Fig. 4F). The channels (between the walls) provided an increased free path for mobile dislocations; hence, contributing to cyclic softening. This observation substantiates the previous hypothesis on the cyclic softening mechanism (*i.e.*, dislocations rearrangement into substructures (Heczko et al., 2021; Lu et al., 2021b)). Besides, the reduction of dislocation density in slip bands (by cross slip) could also lead to cyclic softening. Notably, the presence of slip bands and wall substructures can also allow to rationalize the pronounced Bauschinger effect (see Fig. S4). This effect appears more apparent in the CoCrNi MPEA (whose tension peak stresses are higher than the compression ones) than in conventional 316 L austenitic steels (whose tension and compression peak stresses have similar magnitudes (Oliveira et al., 2022)).

At the near-steady-state stage (close to the end-life), dislocation walls or cells (and in-between channels) become well-organized. Interestingly, the observed screw and partial dislocations (along with bounding SFs) in the channels (see Fig. S5A and Fig. 7B) indicate the important role of both cross slip and planar slip during the majority of CoCrNi's fatigue life. This is distinct from medium-to-high-

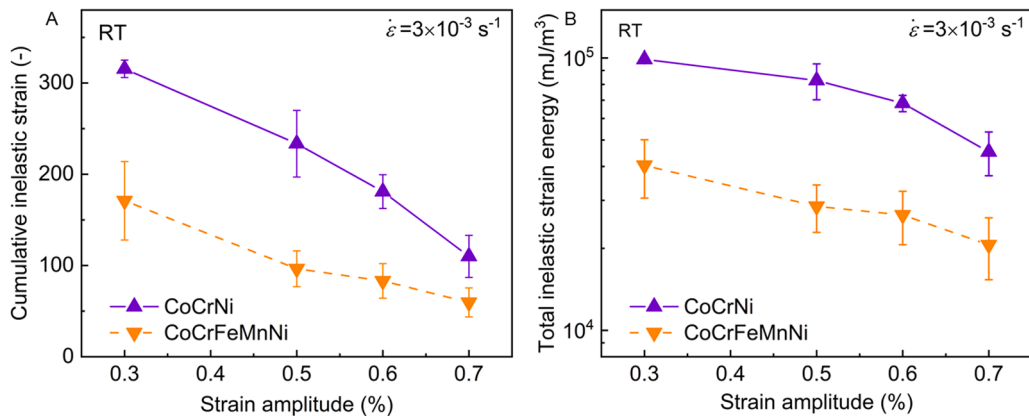


Fig. 9. Comparison between CoCrNi and CoCrFeMnNi: (A) cumulative inelastic strain ($\epsilon_{\text{cum}} = 2\Delta\epsilon_{\text{in}} \bullet N_f$) and (B) total inelastic strain energy (calculated as the sum of the areas of the hysteresis loops) to failure, as a function of strain amplitude. Here, $\Delta\epsilon_{\text{in}}$ is the width of the hysteresis loop, and N_f is the fatigue life. The data of $\Delta\epsilon_{\text{in}}$ and N_f are acquired from our previous work (Lu et al., 2021b). The lines in (A-B) are guidelines to the eye only.

SFE materials (such as CoCrFeMnNi), where only cross slip of screw dislocations dominates (Lu et al., 2021a; Mughrabi, 1983). Therefore, the planar movement of partials and SFs in the low-SFE MPEAs may be responsible for their longer fatigue life (Lu et al., 2021b) and higher fracture toughness (Liu et al., 2022) than those with relatively higher SFEs (such as CoCrFeMnNi).

The beneficial effect of planar slip to fatigue life can be understood in terms of so-called cyclic slip reversibility. As mentioned in (Mughrabi, 2013), in materials in which cross slip is easy, the plastic strain is more irreversible as compared to those dominated by planar slip. This is because cross slip often leads to dislocation annihilations upon one half cycle loading, which is less reversible upon the subsequent reverse half-cycle loading as compared to the current planar slip (where planar dislocations bounding extended SFs glide on the same plane but along opposite directions upon reversing loading directions) (Mughrabi, 2013). In other words, in this work for CoCrNi, slip steps generated during one half-cycle loading by planar slip can be more easily relieved during the reverse half-cycle loading than those by cross slip. Furthermore, cross slip induced annihilations tend to produce an excess of vacancies formation in materials (Essmann et al., 2006; Polák, 1987). The diffusion of these vacancies from the PSB-walls into the adjacent matrix could promote the formation of intrusions in the PSB-matrix interfaces (Polák, 1987). Therefore, fatigue cracks in materials of extensive cross slip (such as CoCrFeMnNi) tend to initiate and propagate faster as compared to those in materials of planar slip mode. Consequently, the predominant planar movement (by partials and extended SFs) in the CoCrNi explains well its exceptional damage tolerance. Additionally, it is of interest to mention that, along with the higher shear modulus, the more reversible deformation (carried by planar movement of partials and SFs) in the low-SFE CoCrNi MPEAs enables it to accumulate larger cumulative inelastic strain (Fig. 9A) and total inelastic strain energy (Fig. 9B) during cyclic loadings than those in CoCrFeMnNi.

4.4. Relationship between dislocation structures and grain orientations

The current study showcased that distinct dislocation patterns after fatigue are weakly dependent on grain orientations in CoCrNi (Fig. 6), akin to observations in CoCrFeMnNi (Lu et al., 2021a). However, this finding differs from other observations in low-SFE materials (Li et al., 2019; Vakili et al., 2020). For instance, for the Fe₅₀Mn₃₀Co₁₀Cr₁₀ MPEA, <102> and <111> oriented grains are preferred for the development of dislocation cells and HDDWs, respectively (Vakili et al., 2020). This was attributed to the <102> grains' higher Schmid factor of perfect dislocations, and the <111> grains' higher Schmid factor for partial dislocations (Vakili et al., 2020). However, in this study, it can be concluded that Schmid factors (for perfect or partial dislocations) alone are insufficient to account for distinct dislocation patterns in different grains in CoCrNi, based on the following observations: (i) the HDDWs are more often observed under a low strain amplitude (0.3%); (ii) both cells and walls are believed to result from cross slip of perfect dislocations, especially under larger strain amplitudes (Mughrabi, 1983); (iii) once cells and walls formed, both perfect and partial dislocations were recognized within the channels (Fig. S5A₁₋₃). Therefore, it is expected that other factors (such as different local stress concentrations as a result of different constraints from adjacent grains (Lu et al., 2021a) and Copley-Kear effect (Copley and Kear, 1968)) may affect the activated slip systems and the resulting dislocation patterns upon cycling CoCrNi.

The Copley-Kear effect also allows to rationalize the coexistence of perfect and partial dislocations (or coexisting cross and planar slips in CoCrNi, see Fig. 6). Specifically, for low-SFE materials (such as a 304 steel with an SFE of 20 mJ/m² (Kestenbach, 1977)), depending on the loading direction (*i.e.*, tension or compression), the separation distance of partial dislocations (or 'effective' SFE) varies, exhibiting either perfect or partial dislocations slip character (Copley and Kear, 1968). For instance, in the current low-SFE CoCrNi, under tension or compression loading, [111] grains may exhibit partial or perfect dislocations slip, respectively (Fig. 6). Therefore, the Copley-Kear effect may play a role in the current low-SFE CoCrNi, leading to the simultaneous presence of partial and perfect dislocations (Fig. S5A₁₋₃); thereby, resulting in the formation of slip bands and walls (or cells) substructures in the same grains (Fig. 5D). Notably, as the simultaneous presence of slip bands and walls (or cells) in the same grains was more frequently observed in CoCrNi alloy (than in CoCrFeMnNi (Lu et al., 2021a)), the Copley-Kear effect plays a more important role in low-SFE alloys.

5. Conclusions

By extensive TEM investigations, this work systematically and statistically unveils the fatigue deformation mechanisms in the prototypical low-SFE CoCrNi MPEA tested at RT and various strain amplitudes (*i.e.*, 0.3%, 0.5% and 0.7%). The key findings can be summarized as follows.

- (1) Under a low strain amplitude of 0.3%, the deformation is accommodated by primary and double planar slip bands (which occupied $\approx 71\%$ and $\approx 29\%$ of grains respectively). These slip bands are suggested to include GNDs.
- (2) With increasing strain amplitude and cycle number, dislocation substructures (including veins, walls, and cells) form due to cross slip despite the low SFE. These substructures are present in up to $\approx 33\%$ and $\approx 60\%$ grains under strain amplitudes of 0.5% and 0.7%, respectively, while the rest of the grains are mainly characterized by the presence of slip bands. It is further suggested that the dislocation walls/cells contain dislocations from multiple-slip systems (rather than primary dislocations), which are majorly SSDs.
- (3) In CoCrNi, the distinct dislocation patterns (including slip bands and veins/walls/cells) were found to be weakly dependent on grain orientation, probably due to local stress concentrations and the Copley-Kear effect.
- (4) Partial dislocations and stacking faults appear to glide within the channels by planar slip (between the walls/cells) in CoCrNi. Despite the presence of walls/cells, the planar slip behavior can accommodate relatively 'more reversible' plastic strain, hence, delaying crack initiation/propagation and contributing to excellent damage tolerance of the CoCrNi. However, this behavior

has not been noticed before in low-SFE alloys and need to be considered more systematically in future using experimental and modeling approaches.

Funding

MS and GL acknowledge funding from the Alexander von Humboldt foundation and the Deutsche Forschungsgemeinschaft through project B8 of the SFB/TR 103, respectively.

Data and materials availability

All data needed to evaluate the conclusions in the paper are present in the paper and/or the Supplementary Material.

Statement of novelty

To the best of our knowledge, there is no existing work (either submitted or already published, including our own) that have a significant overlap with this submission.

CRedit authorship contribution statement

Kaiju Lu: Conceptualization, Methodology, Investigation, Writing – original draft, Visualization. **Ankur Chauhan:** Investigation, Writing – review & editing. **Dimitri Litvinov:** Writing – review & editing. **Mike Schneider:** Resources, Writing – review & editing. **Guillaume Laplanche:** Resources, Writing – review & editing. **Jarir Aktaa:** Resources, Writing – review & editing, Supervision.

Declaration of Competing Interest

The authors declare that they have no known competing financial interests or personal relationships that could have appeared to influence the work reported in this paper.

Data availability

Data will be made available on request.

Acknowledgments

The authors acknowledge Prof. Dr. J. Freudenberger for performing rotary-swaging for the investigated material. KL also thanks Prof. Dr. M. Heilmaier for the helpful suggestions.

References

- Ashby, M.F., 1970. The deformation of plastically non-homogeneous materials. *Philos. Mag.: J. Theor. Exp. Appl. Phys.* 21, 399–424.
- Basinski, Z., Basinski, S., 1992. Fundamental aspects of low amplitude cyclic deformation in face-centred cubic crystals. *Prog. Mater. Sci.* 36, 89–148.
- Buque, C., 2001. Persistent slip bands in cyclically deformed nickel polycrystals. *Int. J. Fatigue* 23, 459–466.
- Calcagnotto, M., Ponge, D., Demir, E., Raabe, D., 2010. Orientation gradients and geometrically necessary dislocations in ultrafine grained dual-phase steels studied by 2D and 3D EBSD. *Mater. Sci. Eng.: A* 527, 2738–2746.
- Cantor, B., Chang, I.T.H., Knight, P., Vincent, A.J.B., 2004. Microstructural development in equiatomic multicomponent alloys. *Mater. Sci. Eng.: A* 375–377, 213–218.
- Cao, P., 2022. Maximum strength and dislocation patterning in multi-principal element alloys. *Sci. Adv.* eabq7433.
- Copley, S.M., Kear, B.H., 1968. The dependence of the width of a dissociated dislocation on dislocation velocity. *Acta Metall.* 16, 227–231.
- Essmann, U., Gösele, U., Mughrabi, H., 2006. A model of extrusions and intrusions in fatigued metals I. Point-defect production and the growth of extrusions. *Philos. Mag.* A 44, 405–426.
- Feng, R., Rao, Y., Liu, C., Xie, X., Yu, D., Chen, Y., Ghazisaeidi, M., Ungar, T., Wang, H., An, K., Liaw, P.K., 2021. Enhancing fatigue life by ductile-transformable multicomponent B2 precipitates in a high-entropy alloy. *Nat. Commun.* 12, 3588.
- Gerold, V., Karnthaler, H.P., 1989. On the origin of planar slip in f.c.c. alloys. *Acta Metall.* 37, 2177–2183.
- Gludovatz, B., Hohenwarter, A., Catoor, D., Chang, E.H., George, E.P., Ritchie, R.O., 2014. A fracture-resistant high-entropy alloy for cryogenic applications. *Science* 345, 1153–1158.
- Gludovatz, B., Hohenwarter, A., Thurston, K.V., Bei, H., Wu, Z., George, E.P., Ritchie, R.O., 2016. Exceptional damage-tolerance of a medium-entropy alloy CrCoNi at cryogenic temperatures. *Nat. Commun.* 7, 10602.
- Gludovatz, B., Ritchie, R.O., 2022. Fracture properties of high-entropy alloys. *MRS Bull.* 47, 176–185.

Habiyaremye, F., Guitton, A., Schäfer, F., Scholz, F., Schneider, M., Frenzel, J., Laplanche, G., Maloufi, N., 2021. Plasticity induced by nanoindentation in a CrCoNi medium-entropy alloy studied by accurate electron channeling contrast imaging revealing dislocation-low angle grain boundary interactions. *Mater. Sci. Eng.: A* 817, 141364.

Heczko, M., Mazánová, V., Slone, C.E., Shih, M., George, E.P., Ghazisaeidi, M., Polák, J., Mills, M.J., 2021. Role of deformation twinning in fatigue of CrCoNi medium-entropy alloy at room temperature. *Scr. Mater.* 202, 113985.

Heczko, M., Polák, J., Kruml, T., 2017. Microstructure and dislocation arrangements in Sanicro 25 steel fatigued at ambient and elevated temperatures. *Mater. Sci. Eng.: A* 680, 168–181.

Hong, S.I., Laird, C., 1990. Mechanisms of slip mode modification in F.C.C. solid solutions. *Acta Metall. Mater.* 38, 1581–1594.

Hua, D., Xia, Q., Wang, W., Zhou, Q., Li, S., Qian, D., Shi, J., Wang, H., 2021. Atomistic insights into the deformation mechanism of a CoCrNi medium entropy alloy under nanoindentation. *Int. J. Plast.* 142, 102997.

Hull, D., Bacon, D.J., 2001. *Introduction to Dislocations*. Butterworth-Heinemann, Amsterdam, Boston, Heidelberg, London, New York, Paris, San Diego, San Francisco, Singapore, Sydney, Tokyo.

Inui, H., Hong, S.I., Laird, C., 1990. A TEM study of dislocation structures in fatigued Cu-16 at.% Al single crystals. *Acta Metall. Mater.* 38, 2261–2274.

Jiang, J., Britton, T.B., Wilkinson, A.J., 2013. Evolution of dislocation density distributions in copper during tensile deformation. *Acta Mater.* 61, 7227–7239.

Kestenbach, H.J., 1977. The effect of applied stress on partial dislocation separation and dislocation substructure in austenitic stainless steel. *Philos. Mag.: J. Theor. Exp. Appl. Phys.* 36, 1509–1515.

Laplanche, G., Gadaud, P., Bärsch, C., Demtröder, K., Reinhart, C., Schreuer, J., George, E.P., 2018. Elastic moduli and thermal expansion coefficients of medium-entropy subsystems of the CrMnFeCoNi high-entropy alloy. *J. Alloys Compd.* 746, 244–255.

Laplanche, G., Kostka, A., Horst, O., Eggeler, G., George, E.P., 2016. Microstructure evolution and critical stress for twinning in the CrMnFeCoNi high-entropy alloy. *Acta Mater.* 118, 152–163.

Laplanche, G., Kostka, A., Reinhart, C., Hunfeld, J., Eggeler, G., George, E.P., 2017. Reasons for the superior mechanical properties of medium-entropy CrCoNi compared to high-entropy CrMnFeCoNi. *Acta Mater.* 128, 292–303.

Laplanche, G., Schneider, M., Scholz, F., Frenzel, J., Eggeler, G., Schreuer, J., 2020. Processing of a single-crystalline CrCoNi medium-entropy alloy and evolution of its thermal expansion and elastic stiffness coefficients with temperature. *Scr. Mater.* 177, 44–48.

Lavenstein, S., Gu, Y., Madiseti, D., El-Adawy, J.A., 2020. The heterogeneity of persistent slip band nucleation and evolution in metals at the micrometer scale. *Science* 370, eabb2690.

Li, L., Chen, Z., Kuroiwa, S., Ito, M., Yuge, K., Kishida, K., Tanimoto, H., Yu, Y., Inui, H., George, E.P., 2022. Evolution of short-range order and its effects on the plastic deformation behavior of single crystals of the equiatomic Cr-Co-Ni medium-entropy alloy. *Acta Mater.*

Li, P., Li, S., Wang, Z., Zhang, Z., 2011. Fundamental factors on formation mechanism of dislocation arrangements in cyclically deformed fcc single crystals. *Prog. Mater. Sci.* 56, 328–377.

Li, R., Wang, Y.-D., Liu, W., Geng, C., Xie, Q., Brown, D.E., An, K., 2019. Multiscale mechanical fatigue damage of stainless steel investigated by neutron diffraction and X-ray microdiffraction. *Acta Mater.* 165, 336–345.

Li, Y., Laird, C., 1994. Cyclic response and dislocation structures of AISI 316L stainless steel. Part 2: polycrystals fatigued at intermediate strain amplitude. *Mater. Sci. Eng.: A* 186, 87–103.

Liu, D., Yu, Q., Kabra, S., Jiang, M., Forna-Kreutzer, P., Zhang, R., Payne, M., Walsh, F., Gludovatz, B., Asta, M., Minor, A.M., George, E.P., Ritchie, R.O., 2022. Exceptional fracture toughness of CrCoNi-based medium- and high-entropy alloys at 20 kelvin. *Science* 378, 978–983.

Lu, K., Chauhan, A., Litvinov, D., Aktaa, J., 2022a. Temperature-dependent cyclic deformation behavior of CoCrFeMnNi high-entropy alloy. *Int. J. Fatigue* 160, 106863.

Lu, K., Chauhan, A., Litvinov, D., Walter, M., Tirunilai, A.S., Freudenberger, J., Kauffmann, A., Heilmaier, M., Aktaa, J., 2020. High-temperature low cycle fatigue behavior of an equiatomic CoCrFeMnNi high-entropy alloy. *Mater. Sci. Eng.: A* 791, 139781.

Lu, K., Chauhan, A., Tirunilai, A.S., Freudenberger, J., Kauffmann, A., Heilmaier, M., Aktaa, J., 2021a. Deformation mechanisms of CoCrFeMnNi high-entropy alloy under low-cycle-fatigue loading. *Acta Mater.* 215, 117089.

Lu, K., Chauhan, A., Walter, M., Tirunilai, A.S., Schneider, M., Laplanche, G., Freudenberger, J., Kauffmann, A., Heilmaier, M., Aktaa, J., 2021b. Superior low-cycle fatigue properties of CoCrNi compared to CoCrFeMnNi. *Scr. Mater.* 194, 113667.

Lu, K., Knöpfle, F., Chauhan, A., Jeong, H.T., Litvinov, D., Walter, M., Kim, W.J., Aktaa, J., 2022b. Low-cycle fatigue behavior and deformation mechanisms of a dual-phase Al_{0.5}CoCrFeMnNi high-entropy alloy. *Int. J. Fatigue* 163, 107075.

Luo, M.-Y., Lam, T.-N., Wang, P.-T., Tsou, N.-T., Chang, Y.-J., Feng, R., Kawasaki, T., Harjo, S., Liaw, P.K., Yeh, A.-C., Lee, S.Y., Jain, J., Huang, E.W., 2022. Grain-size-dependent microstructure effects on cyclic deformation mechanisms in CoCrFeMnNi high-entropy-alloys. *Scr. Mater.* 210, 114459.

Mayama, T., Sasaki, K., Kuroda, M., 2008. Quantitative evaluations for strain amplitude dependent organization of dislocation structures due to cyclic plasticity in austenitic stainless steel 316L. *Acta Mater.* 56, 2735–2743.

Mecking, H., Kocks, U.F., 1981. Kinetics of flow and strain-hardening. *Acta Metall.* 29, 1865–1875.

Meyers, M.A., Vöhringer, O., Lubarda, V.A., 2001. The onset of twinning in metals: a constitutive description. *Acta Mater.* 49, 4025–4039.

Ming, K., Li, L., Li, Z., Bi, X., Wang, J., 2019. Grain boundary decohesion by nanoclustering Ni and Cr separately in CrMnFeCoNi high-entropy alloys. *Sci. Adv.* 5, eaay0639.

Mughrabi, H., 1983. Dislocation wall and cell structures and long-range internal stresses in deformed metal crystals. *Acta Metall.* 31, 1367–1379.

Mughrabi, H., 2013. Cyclic slip irreversibility and fatigue life: a microstructure-based analysis. *Acta Mater.* 61, 1197–1203.

Mughrabi, H., 2016. The α -factor in the Taylor flow-stress law in monotonic, cyclic and quasi-stationary deformations: dependence on slip mode, dislocation arrangement and density. *Curr. Opin. Solid State Mater. Sci.* 20, 411–420.

Nellessen, J., Sandlöbes, S., Raabe, D., 2015. Effects of strain amplitude, cycle number and orientation on low cycle fatigue microstructures in austenitic stainless steel studied by electron channelling contrast imaging. *Acta Mater.* 87, 86–99.

Okamoto, N.L., Fujimoto, S., Kambara, Y., Kawamura, M., Chen, Z.M., Matsunoshita, H., Tanaka, K., Inui, H., George, E.P., 2016. Size effect, critical resolved shear stress, stacking fault energy, and solid solution strengthening in the CrMnFeCoNi high-entropy alloy. *Sci. Rep.* 6, 35863.

Oliveira, D.M., San Marchi, C.W., Medlin, D.L., Gibeling, J.C., 2022. The influence of hydrogen on the low cycle fatigue behavior of strain-hardened 316L stainless steel. *Mater. Sci. Eng.: A* 849, 143477.

Pan, Q., Zhang, L., Feng, R., Lu, Q., An, K., Chuang, A.C., Poplawsky, J.D., Liaw, P.K., Lu, L., 2021. Gradient-cell-structured high-entropy alloy with exceptional strength and ductility. *Science* 0, eabj8114.

Pham, M.S., Holdsworth, S.R., Janssens, K.G.F., Mazza, E., 2013. Cyclic deformation response of AISI 316L at room temperature: mechanical behaviour, microstructural evolution, physically-based evolutionary constitutive modelling. *Int. J. Plast.* 47, 143–164.

Picak, S., Wegener, T., Sajadifar, S.V., Sobrero, C., Richter, J., Kim, H., Niendorf, T., Karaman, I., 2020. On the low cycle fatigue response of CoCrNiFeMn high entropy alloy with ultra-fine grain structure. *Acta Mater.* 205, 116540.

Polák, J., 1987. On the role of point defects in fatigue crack initiation. *Mater. Sci. Eng.* 92, 71–80.

Polák, J., Petráš, R., Heczko, M., Kuběna, I., Kruml, T., Chai, G., 2014. Low cycle fatigue behavior of Sanicro25 steel at room and at elevated temperature. *Mater. Sci. Eng.: A* 615, 175–182.

Sangid, M.D., 2013. The physics of fatigue crack initiation. *Int. J. Fatigue* 57, 58–72.

Schneider, M., George, E.P., Manescau, T.J., Zálezák, T., Hunfeld, J., Dlouhy, A., Eggeler, G., Laplanche, G., 2019. Benchmark dataset of the effect of grain size on strength in the single-phase FCC CrCoNi medium entropy alloy. *Data Brief* 27, 104592.

Schneider, M., George, E.P., Manescau, T.J., Zálezák, T., Hunfeld, J., Dlouhy, A., Eggeler, G., Laplanche, G., 2020. Analysis of strengthening due to grain boundaries and annealing twin boundaries in the CrCoNi medium-entropy alloy. *Int. J. Plast.* 124, 155–169.

- Shams, S.A.A., Jang, G., Won, J.W., Bae, J.W., Jin, H., Kim, H.S., Lee, C.S., 2020. Low-cycle fatigue properties of CoCrFeMnNi high-entropy alloy compared with its conventional counterparts. *Mater. Sci. Eng.: A* 792, 139661.
- Shao, C.W., Zhang, P., Liu, R., Zhang, Z.J., Pang, J.C., Duan, Q.Q., Zhang, Z.F., 2016. A remarkable improvement of low-cycle fatigue resistance of high-Mn austenitic TWIP alloys with similar tensile properties: importance of slip mode. *Acta Mater.* 118, 196–212.
- Shao, C.W., Zhang, P., Zhu, Y.K., Zhang, Z.J., Pang, J.C., Zhang, Z.F., 2017. Improvement of low-cycle fatigue resistance in TWIP steel by regulating the grain size and distribution. *Acta Mater.* 134, 128–142.
- Shih, M., Miao, J., Mills, M., Ghazisaeidi, M., 2021. Stacking fault energy in concentrated alloys. *Nat. Commun.* 12, 3590.
- Sisodia, S., Rajkowski, M., Laplanche, G., Chauhan, A., 2023. Cyclic deformation behavior of an equiatomic CrFeNi multi-principal element alloy. *Int. J. Fatigue* 174, 107723.
- Stinville, J.C., Charpagne, M.A., Cervellon, A., Hemery, S., Wang, F., Callahan, P.G., Valle, V., Pollock, T.M., 2022. On the origins of fatigue strength in crystalline metallic materials. *Science* 377, 1065–1071.
- Suresh, S., 1998. *Fatigue of Materials*. Cambridge University Press, Cambridge.
- Vakili, S.M., Zarei-Hanzaki, A., Anoushe, A.S., Abedi, H.R., Mohammad-Ebrahimi, M.H., Jaskari, M., Sohn, S.S., Ponge, D., Karjalainen, L.P., 2020. Reversible dislocation movement, martensitic transformation and nano-twinning during elastic cyclic loading of a metastable high entropy alloy. *Acta Mater.* 185, 474–492.
- Wagner, C., Ferrari, A., Schreuer, J., Couzinié, J.-P., Ikeda, Y., Körmann, F., Eggeler, G., George, E.P., Laplanche, G., 2022. Effects of Cr/Ni ratio on physical properties of Cr-Mn-Fe-Co-Ni high-entropy alloys. *Acta Mater.* 227, 117693.
- Wagner, C., Laplanche, G., 2023a. Effect of grain size on critical twinning stress and work hardening behavior in the equiatomic CrMnFeCoNi high-entropy alloy. *Int. J. Plast.* 166, 103651.
- Wagner, C., Laplanche, G., 2023b. Effects of stacking fault energy and temperature on grain boundary strengthening, intrinsic lattice strength and deformation mechanisms in CrMnFeCoNi high-entropy alloys with different Cr/Ni ratios. *Acta Mater.* 244, 118541.
- Williams, D.B., Carter, C.B., 1996. *The Transmission Electron Microscope, Transmission Electron Microscopy*. Springer, New York, pp. 3–17.
- Winter, A., Pedersen, O., Rasmussen, K., 1981. Dislocation microstructures in fatigued copper polycrystals. *Acta Metall.* 29, 735–748.
- Yan, B.D., Cheng, A.S., Buchinger, L., Stanzl, S., Laird, C., 1986. The cyclic stress—strain response of single crystals of Cu-16 at.%Al alloy I: cyclic hardening and strain localization. *Mater. Sci. Eng.* 80, 129–142.
- Zhang, R., Zhao, S., Ding, J., Chong, Y., Jia, T., Ophus, C., Asta, M., Ritchie, R.O., Minor, A.M., 2020. Short-range order and its impact on the CrCoNi medium-entropy alloy. *Nature* 581, 283–287.
- Zhi, H., Zhang, C., Antonov, S., Yu, H., Guo, T., Su, Y., 2020. Investigations of dislocation-type evolution and strain hardening during mechanical twinning in Fe-22Mn-0.6C twinning-induced plasticity steel. *Acta Mater.* 195, 371–382.
- Zhu, C., Harrington, T., Gray, G.T., Vecchio, K.S., 2018. Dislocation-type evolution in quasi-statically compressed polycrystalline nickel. *Acta Mater.* 155, 104–116.